Optics EXPRESS

Influence of hydration water on $CH_3NH_3PbI_3$ perovskite films prepared through one-step procedure

ZIYI WANG,[1] SIJIAN YUAN,[2] DAHAI LI,[1] FENG JIN,[1] RONGJUN ZHANG,[1,5] YIQIANG ZHAN,[2,6] MING LU,[1] SONGYOU WANG,[1] YUXIANG ZHENG,[1] JUNPENG GUO,[3] ZHIYONG FAN,[4] AND LIANGYAO CHEN[1]

[1]*Key Laboratory of Micro and Nano Photonic Structures, Ministry of Education, Department of Optical Science and Engineering, Fudan University, Shanghai 200433, China*
[2]*State Key Laboratory of ASIC and System, SIST, Fudan University, Shanghai 200433, China*
[3]*Department of Electrical and Computer Engineering, University of Alabama in Huntsville, 301 Sparkman Dr., Huntsville, Alabama 35899, USA*
[4]*Department of Electronic and Computer Engineering, Hong Kong University of Science and Technology, Hong Kong SAR, China*
[5]*rjzhang@fudan.edu.cn*
[6]*yqzhan@fudan.edu.cn*

Abstract: Organic-inorganic perovskites were fabricated through a one-step procedure with different levels of hydration water in precursor solutions. The optical properties of $CH_3NH_3PbI_3$ films were investigated through spectroscopic ellipsometry and photoluminescence measurements. With the measured optical constants, the efficiency limit of perovskite solar cells is predicted with a detailed balance model. By comparing the optical measurement to that of planar heterojunction solar cells, we conclude that the radiative efficiency and porosity of the perovskite film significantly influence the performance of perovskite solar cells. An optimized hydration-water concentration is obtained for the $3CH_3NH_3I{:}1PbAc_2{\bullet}xH_2O$ precursor solution. The results can provide guidance for further optimization of the device performance of perovskite solar cells by utilizing hydration water.

OCIS codes: (310.6860) Thin films, optical properties; (160.0160) Materials; (350.6050) Solar energy.

References and links

1. A. Kojima, K. Teshima, Y. Shirai, and T. Miyasaka, "Organometal halide perovskites as visible-light sensitizers for photovoltaic cells," J. Am. Chem. Soc. **131**(17), 6050–6051 (2009).
2. M. A. Green, K. Emery, Y. Hishikawa, W. Warta, and E. D. Dunlop, "Solar cell efficiency tables (version 46)," Prog. Photovolt. Res. Appl. **23**(7), 805–812 (2015).
3. Y. Zhao, M.-Y. Sheng, W.-X. Zhou, Y. Shen, E.-T. Hu, J.-B. Chen, M. Xu, Y.-X. Zheng, Y.-P. Lee, D. W. Lynch, and L. Y. Chen, "A solar photovoltaic system with ideal efficiency close to the theoretical limit," Opt. Express **20**(1), A28–A38 (2012).
4. E. D. Kosten, J. H. Atwater, J. Parsons, A. Polman, and H. A. Atwater, "Highly efficient GaAs solar cells by limiting light emission angle," Light Sci. Appl. **2**(1), e45 (2013).
5. Z. Y. Wang, R. J. Zhang, S. Y. Wang, M. Lu, X. Chen, Y. X. Zheng, L. Y. Chen, Z. Ye, C. Z. Wang, and K. M. Ho, "Broadband optical absorption by tunable Mie resonances in silicon nanocone arrays," Sci. Rep. **5**, 7810 (2015).
6. M. Filipič, P. Löper, B. Niesen, S. De Wolf, J. Krč, C. Ballif, and M. Topič, "$CH_3NH_3PbI_3$perovskite / silicon tandem solar cells: characterization based optical simulations," Opt. Express **23**(7), A263–A278 (2015).
7. G. Niu, X. Guo, and L. Wang, "Review of recent progress in chemical stability of perovskite solar cells," J. Mater. Chem. A Mater. Energy Sustain. **3**(17), 8970–8980 (2015).
8. W. Nie, H. Tsai, R. Asadpour, J.-C. Blancon, A. J. Neukirch, G. Gupta, J. J. Crochet, M. Chhowalla, S. Tretiak, M. A. Alam, H. L. Wang, and A. D. Mohite, "Solar cells. High-efficiency solution-processed perovskite solar cells with millimeter-scale grains," Science **347**(6221), 522–525 (2015).
9. M. Liu, M. B. Johnston, and H. J. Snaith, "Efficient planar heterojunction perovskite solar cells by vapour deposition," Nature **501**(7467), 395–398 (2013).

#273045 http://dx.doi.org/10.1364/OE.24.0A1431
Journal © 2016 Received 9 Aug 2016; revised 19 Sep 2016; accepted 21 Sep 2016; published 30 Sep 2016

10. K. Fu, C. T. Nelson, M. C. Scott, A. Minor, N. Mathews, and L. H. Wong, "Influence of void-free perovskite capping layer on the charge recombination process in high performance $CH_3NH_3PbI_3$ perovskite solar cells," Nanoscale **8**(7), 4181–4193 (2016).
11. Q. Chen, H. Zhou, Z. Hong, S. Luo, H.-S. Duan, H.-H. Wang, Y. Liu, G. Li, and Y. Yang, "Planar heterojunction perovskite solar cells via vapor-assisted solution process," J. Am. Chem. Soc. **136**(2), 622–625 (2014).
12. P. W. Liang, C. Y. Liao, C. C. Chueh, F. Zuo, S. T. Williams, X. K. Xin, J. Lin, and A. K. Y. Jen, "Additive enhanced crystallization of solution-processed perovskite for highly efficient planar-heterojunction solar cells," Adv. Mater. **26**(22), 3748–3754 (2014).
13. J. Burschka, N. Pellet, S.-J. Moon, R. Humphry-Baker, P. Gao, M. K. Nazeeruddin, and M. Grätzel, "Sequential deposition as a route to high-performance perovskite-sensitized solar cells," Nature **499**(7458), 316–319 (2013).
14. M. Xiao, F. Huang, W. Huang, Y. Dkhissi, Y. Zhu, J. Etheridge, A. Gray-Weale, U. Bach, Y. B. Cheng, and L. Spiccia, "A fast deposition-crystallization procedure for highly efficient lead iodide perovskite thin-film solar cells," Angew. Chem. Int. Ed. Engl. **53**(37), 9898–9903 (2014).
15. W. Zhang, M. Saliba, D. T. Moore, S. K. Pathak, M. T. Hörantner, T. Stergiopoulos, S. D. Stranks, G. E. Eperon, J. A. Alexander-Webber, A. Abate, A. Sadhanala, S. Yao, Y. Chen, R. H. Friend, L. A. Estroff, U. Wiesner, and H. J. Snaith, "Ultrasmooth organic-inorganic perovskite thin-film formation and crystallization for efficient planar heterojunction solar cells," Nat. Commun. **6**, 6142 (2015).
16. L. Ling, S. Yuan, P. Wang, H. Zhang, L. Tu, J. Wang, Y. Zhan, and L. Zheng, "Hydration water improved organic-inorganic perovskite layer for efficient planar solar cell," Adv. Funct. Mater. in press.
17. E. Wei, X. Ren, L. Chen, and W. C. Choy, "The efficiency limit of $CH_3NH_3PbI_3$ perovskite solar cells," Appl. Phys. Lett. **106**(22), 221104 (2015).
18. M. Shirayama, H. Kadowaki, T. Miyadera, T. Sugita, M. Tamakoshi, M. Kato, T. Fujiseki, D. Murata, S. Hara, T. N. Murakami, S. Fujimoto, M. Chikamatsu, and H. Fujiwara, "Optical transitions in hybrid perovskite solar cells: ellipsometry, density functional theory, and quantum efficiency analyses for $CH_3NH_3PbI_3$," Phys. Rev. Appl. **5**(1), 014012 (2016).
19. P. Löper, M. Stuckelberger, B. Niesen, J. Werner, M. Filipič, S.-J. Moon, J.-H. Yum, M. Topič, S. De Wolf, and C. Ballif, "Complex refractive index spectra of $CH_3NH_3PbI_3$ perovskite thin films determined by spectroscopic ellipsometry and spectrophotometry," J. Phys. Chem. Lett. **6**(1), 66–71 (2015).
20. X. Ziang, L. Shifeng, Q. Laixiang, P. Shuping, W. Wei, Y. Yu, Y. Li, C. Zhijian, W. Shufeng, D. Honglin, Y. Minghui, and G. G. Qin, "Refractive index and extinction coefficient of $CH_3NH_3PbI_3$ studied by spectroscopic ellipsometry," Opt. Mater. Express **5**(1), 29–43 (2015).
21. J. M. Ball, S. D. Stranks, M. T. Hörantner, S. Hüttner, W. Zhang, E. J. Crossland, I. Ramirez, M. Riede, M. B. Johnston, R. H. Friend, and H. J. Snaith, "Optical properties and limiting photocurrent of thin-film perovskite solar cells," Energy Environ. Sci. **8**(2), 602–609 (2015).
22. J.-S. Park, S. Choi, Y. Yan, Y. Yang, J. M. Luther, S.-H. Wei, P. Parilla, and K. Zhu, "Electronic structure and optical properties of α-$CH_3NH_3PbBr_3$ perovskite single crystal," J. Phys. Chem. Lett. **6**(21), 4304–4308 (2015).
23. C.-W. Chen, S.-Y. Hsiao, C.-Y. Chen, H.-W. Kang, Z.-Y. Huang, and H.-W. Lin, "Optical properties of organometal halide perovskite thin films and general device structure design rules for perovskite single and tandem solar cells," J. Mater. Chem. A Mater. Energy Sustain. **3**(17), 9152–9159 (2015).
24. A. M. A. Leguy, P. Azarhoosh, M. I. Alonso, M. Campoy-Quiles, O. J. Weber, J. Yao, D. Bryant, M. T. Weller, J. Nelson, A. Walsh, M. van Schilfgaarde, and P. R. F. Barnes, "Experimental and theoretical optical properties of methylammonium lead halide perovskites," Nanoscale **8**(12), 6317–6327 (2016).
25. H. Zhou, Q. Chen, G. Li, S. Luo, T. B. Song, H.-S. Duan, Z. Hong, J. You, Y. Liu, and Y. Yang, "Photovoltaics. Interface engineering of highly efficient perovskite solar cells," Science **345**(6196), 542–546 (2014).
26. G. E. Eperon, S. N. Habisreutinger, T. Leijtens, B. J. Bruijnaers, J. J. van Franeker, D. W. deQuilettes, S. Pathak, R. J. Sutton, G. Grancini, D. S. Ginger, R. A. Janssen, A. Petrozza, and H. J. Snaith, "The importance of moisture in hybrid lead halide perovskite thin film fabrication," ACS Nano **9**(9), 9380–9393 (2015).
27. H. Fujiwara, *Spectroscopic Ellipsometry: Principles and Applications* (John Wiley and Sons, 2007).
28. R. L. Olmon, B. Slovick, T. W. Johnson, D. Shelton, S.-H. Oh, G. D. Boreman, and M. B. Raschke, "Optical dielectric function of gold," Phys. Rev. B **86**(23), 235147 (2012).
29. D. Zhang, B. Shen, Y. Zheng, S. Wang, J. Zhang, S. Yang, R. Zhang, L. Chen, C. Wang, and K. Ho, "Evolution of optical properties of tin film from solid to liquid studied by spectroscopic ellipsometry and ab initio calculation," Appl. Phys. Lett. **104**(12), 121907 (2014).
30. L. Jian and C. Jie, "Broadening of optical transitions in polycrystalline CdS and CdTe thin films," Appl. Phys. Lett. **97**(18), 181909 (2010).
31. J.-P. Xu, R.-J. Zhang, Y. Zhang, Z.-Y. Wang, L. Chen, Q.-H. Huang, H.-L. Lu, S.-Y. Wang, Y.-X. Zheng, and L.-Y. Chen, "The thickness-dependent band gap and defect features of ultrathin ZrO_2 films studied by spectroscopic ellipsometry," Phys. Chem. Chem. Phys. **18**(4), 3316–3321 (2016).
32. Z.-Y. Wang, R.-J. Zhang, H.-L. Lu, X. Chen, Y. Sun, Y. Zhang, Y.-F. Wei, J.-P. Xu, S.-Y. Wang, Y.-X. Zheng, and L. Y. Chen, "The impact of thickness and thermal annealing on refractive index for aluminum oxide thin films deposited by atomic layer deposition," Nanoscale Res. Lett. **10**(1), 46 (2015).
33. R.-J. Zhang, Y.-M. Chen, W.-J. Lu, Q.-Y. Cai, Y.-X. Zheng, and L.-Y. Chen, "Influence of nanocrystal size on dielectric functions of Si nanocrystals embedded in SiO_2 matrix," Appl. Phys. Lett. **95**(16), 161109 (2009).

34. G. Q. Xia, R. J. Zhang, Y. L. Chen, H. B. Zhao, S. Y. Wang, S. M. Zhou, Y. X. Zheng, Y. M. Yang, L. Y. Chen, J. H. Chu, and Z. M. Wang, "New design of the variable angle infrared spectroscopic ellipsometer using double Fourier transforms," Rev. Sci. Instrum. **71**(7), 2677–2683 (2000).
35. W.-J. Yin, J.-H. Yang, J. Kang, Y. Yan, and S.-H. Wei, "Halide perovskite materials for solar cells: a theoretical review," J. Mater. Chem. A Mater. Energy Sustain. **3**(17), 8926–8942 (2015).
36. J. Even, L. Pedesseau, C. Katan, M. Kepenekian, J.-S. Lauret, D. Sapori, and E. Deleporte, "Solid-state physics perspective on hybrid perovskite semiconductors," J. Phys. Chem. C **119**(19), 10161–10177 (2015).
37. S. Pathak, A. Sepe, A. Sadhanala, F. Deschler, A. Haghighirad, N. Sakai, K. C. Goedel, S. D. Stranks, N. Noel, M. Price, S. Hüttner, N. A. Hawkins, R. H. Friend, U. Steiner, and H. J. Snaith, "Atmospheric influence upon crystallization and electronic disorder and its impact on the photophysical properties of organic-inorganic perovskite solar cells," ACS Nano **9**(3), 2311–2320 (2015).
38. T. Baikie, Y. Fang, J. M. Kadro, M. Schreyer, F. Wei, S. G. Mhaisalkar, M. Graetzel, and T. J. White, "Synthesis and crystal chemistry of the hybrid perovskite (CH_3NH_3) PbI_3 for solid-state sensitised solar cell applications," J. Mater. Chem. A Mater. Energy Sustain. **1**(18), 5628–5641 (2013).
39. H. Fujiwara, J. Koh, P. Rovira, and R. Collins, "Assessment of effective-medium theories in the analysis of nucleation and microscopic surface roughness evolution for semiconductor thin films," Phys. Rev. B **61**(16), 10832–10844 (2000).
40. G. E. Jellison and F. A. Modine, "Parameterization of the optical functions of amorphous materials in the interband region," Appl. Phys. Lett. **69**(3), 371–373 (1996).
41. M. A. Green, Y. Jiang, A. M. Soufiani, and A. Ho-Baillie, "Optical properties of photovoltaic organic–inorganic lead halide perovskites," J. Phys. Chem. Lett. **6**(23), 4774–4785 (2015).
42. E. Doni, G. Grosso, G. Harbeke, E. Meier, and E. Tosatti, "Interlayer interaction and optical properties of layer semiconductors: 2H and 4H polytypes of PbI_2," Phys. Status Solidi **68**(2), 569–574 (1975).
43. W. Shockley and H. J. Queisser, "Detailed balance limit of efficiency of p-n junction solar cells," J. Appl. Phys. **32**(3), 510–519 (1961).
44. D. Shi, Y. Zeng, and W. Shen, "Perovskite/c-Si tandem solar cell with inverted nanopyramids: realizing high efficiency by controllable light trapping," Sci. Rep. **5**, 16504 (2015).
45. M. A. Green, "Limits on the open-circuit voltage and efficiency of silicon solar cells imposed by intrinsic Auger processes," IEEE Trans. Electron Dev. **31**(5), 671–678 (1984).
46. S. Agarwal and P. R. Nair, "Device engineering of perovskite solar cells to achieve near ideal efficiency," Appl. Phys. Lett. **107**(12), 123901 (2015).
47. U. Rau, "Reciprocity relation between photovoltaic quantum efficiency and electroluminescent emission of solar cells," Phys. Rev. B **76**(8), 085303 (2007).
48. K. Tvingstedt, O. Malinkiewicz, A. Baumann, C. Deibel, H. J. Snaith, V. Dyakonov, and H. J. Bolink, "Radiative efficiency of lead iodide based perovskite solar cells," Sci. Rep. **4**, 6071 (2014).

1. Introduction

During the past several years, solar cells based on methylammonium lead iodide ($CH_3NH_3PbI_3$) perovskite have attracted much attention because of their high energy conversion efficiency [1]. The power-conversion efficiency (PCE) of perovskite-based solar cells has rapidly increased to exceed 20% [2]. The most common methods to increase the PCE of solar cells are structure optimization [3–6] and film-quality improvement [7]. The quality of perovskite films has been improved using various methods such as large grain growth [8], surface smoothening [9, 10], defect passivation [11, 12], and process optimization [13, 14]. It has been reported that ultra-smooth and nearly pinhole-free $CH_3NH_3PbI_3$ films can be achieved using lead acetate ($PbAc_2$) instead of lead halides [15]. Further, controlling the content of hydration water in precursors can significantly improve the smoothness and uniformity of perovskite solar cells [16]. In addition, the use of hydration water can greatly simplify the one-step process of fabricating perovskite films, which enables the future mass production of perovskite solar cells [15, 16].

One of the critical features of perovskite solar cells is that a relatively high short-circuit photocurrent density (J_{sc}) can be easily achieved [17]. In an ideal solar cell, J_{sc} is mainly controlled by the optical absorption of the absorber layer [18]. As the $CH_3NH_3PbI_3$ layer is the critical light absorber in a perovskite solar cell, its optical properties need to be thoroughly studied. There are several reports on the refractive index and extinction coefficient of $CH_3NH_3PbI_3$ [18–24]. However, the previous results are inconsistent with each other. Since the properties of perovskite films are strongly influenced by the precursors and process utilized in fabrication, the perovskite films fabricated using different processes may demonstrate different optical and electronic properties, although the final composition remains constant. Therefore, it is difficult to perform a fair comparison of different perovskite films, and a systematic study of perovskite films fabricated from similar precursors and processes is needed. Interestingly, recently work has shown that the use of hydration-water-controlled precursors can improve the performance of devices based on perovskite [16]. Furthermore, previous studies have demonstrated that moisture can assist the growth of $CH_3NH_3PbI_3$ and lead to better device performance [25, 26]. Therefore, the investigation of the optical properties of hydration-water-improved perovskite films is of significant importance.

Spectroscopic ellipsometry (SE) is an indirect measurement technique routinely used for determining the optical properties of thin films [27]. It features fast and non-destructive detection over a wide photon-energy range, making it suitable for the characterization of many materials including metals [28, 29], semiconductors [30, 31], insulators [32], and nanocrystals [33]. In the SE measurement, two parameters ψ and Δ can be revealed from the expression of complex reflectance ratio ρ [27, 34]:

$$\rho = \tan(\Psi)e^{i\Delta} = \frac{r_p}{r_s}, \tag{1}$$

where r_p and r_s are the Fresnel reflection coefficients of *p*- and *s*- polarized light, respectively. Further, ψ and Δ are the amplitude ratio of reflected *p*- to *s*-polarized light and the phase shift difference, respectively. The ellipsometric spectra can be fitted based on an optical model, which is constructed from the physical structure of the measured sample. Then, the dielectric functions can be solved.

2. Experimental details

2.1 Preparation of $CH_3NH_3PbI_3$ precursor solution

$PbAc_2•3H_2O$ was heated to 100 °C in the glovebox to release the hydration water. $PbAc_2•xH_2O$ was then obtained by mixing $PbAc_2•3H_2O$ with dehydrated $PbAc_2$ at a certain mole ratio. Finally, the $3CH_3NH_3I{:}1PbAc_2•xH_2O$ precursor solutions were generated by dissolving CH_3NH_3I and $PbAc_2•xH_2O$ in anhydrous dimethylformamide (DMF) at a 3:1 molar ratio with the concentration of 35 wt%. The reactions process are as follows [16]:

$$3CH_3NH_3I + PbAc_2•3H_2O \underset{in\ solution}{\overset{40°C}{\rightleftarrows}} CH_3NH_3PbI_3•H_2O + 2H_2O + 2CH_3NH_3Ac_2 \tag{2}$$

$$CH_3NH_3PbI_3•\mathrm{H}_2O \xrightarrow{in\ air} CH_3NH_3PbI_3 + \mathrm{H}_2O \tag{3}$$

2.2 Device fabrication

The solar-cell devices are constructed with a structure of ITO/ PEDOT:PSS/ $CH_3NH_3PbI_3$/ [6, 6]-phenyl-C61-butyric acid-methyl-ester (PBCM)/ C_{60}/ 2,9-dimethyl-4,7-diphenyl-1,10-phenanthroline (BCP)/ Ag. PEDOT:PSS was spin-coated on cleaned ITO substrates at 4,000 rpm. The films were then annealed at 130 °C. Perovskite films were spin-coated from the prepared precursor solutions at 2,000 rpm and then annealed on a hotplate at 100 °C for 5 min. PCBM (dissolved in CB, 20 mg/ml) was spin-coated on top of the perovskite layer at 1,800 rpm. The fabrication of the devices was completed through the thermal evaporation of C_{60}, BCP, and Ag. Detailed information for the solar cells can be found in a previous report by Li et al. [16]. We prepared five solar cells for each hydration-water content, and the solar cells with the highest filling factor were selected for comparison.

2.3 $CH_3NH_3PbI_3$ film characterization

The optical constants of $CH_3NH_3PbI_3$ films, a relatively unstable material, are easily affected by moisture in the environment. To avoid degradation, all samples were sealed in a nitrogen environment until SE measurement. SE measurements (J.A. Woollam, Inc., M2000X-FB-300XTF) were performed from 1.38 to 4.13 eV at room temperature and at an incident angle of 65°. All the SE measurements were completed within 30 s after the exposure of the samples to air.

The photoluminescence (PL) intensity was measured immediately after the SE measurement. A semiconductor laser with a wavelength of 447 nm was used as the pump light. The wavelength of PL was selected using a monochromator, and a long-pass filter (>500 nm) was placed before the monochromator to eliminate the influence of stray light from the pump laser. The PL signal was detected using a Si photodetector combined with a lock-in amplifier.

The film morphologies were determined with a scanning electron microscope (FEI Siron200, SEM) and an atomic force microscope (Bruker Dimension Icon VT-1000 System, AFM) in the tapping mode. The perovskite phases were analyzed using an X-ray diffractometer (Bruker-AXS D8, XRD) with a Cu-Kα radiation source ($\lambda = 1.5406$ Å).

2.4 Solar-cell characterization

J-V curves were measured using an electrochemical workstation (ZAHNER CIMPS) under AM1.5 sunlight at 100 mV/m^2 irradiance generated by a Class AAA sun simulator (SF300-A Sciencetech-Inc.). A Si diode (Hamamatsu S1133) was used to calibrate the light intensity and stability. The solar cells were masked with a 3D-printed aperture to define the active area.

3. Results and discussions

To investigate the influence of hydration water on the formation of $CH_3NH_3PbI_3$ through the one-step method from a 3:1 solution (by moles) of $CH_3NH_3I{:}PbAc_2{\bullet}xH_2O$ in DMF precursor solutions, five $CH_3NH_3PbI_3$ samples were fabricated on quartz/ PEDOT: PSS substrates. The content of hydration water was carefully controlled in $3CH_3NH_3I{:}1PbAc_2{\bullet}xH_2O$ with x equals to 0, 0.75, 1.50, 2.25, and 3.00. Figure 1 illustrates the morphology of $CH_3NH_3PbI_3$ films measured by AFM and SEM. The values of root-mean-square roughness (RMS roughness, R_q) of the five samples were 14.1, 12.2, 10.7, 10.7, and 10.8 nm, respectively. The flat surfaces of $CH_3NH_3PbI_3$ films enable SE measurements [18, 23], and the surface roughness decreased with the increasing content of hydration water in $PbAc_2$ until it reaches $x = 1.50$ from $x = 0$, which indicates that hydration water plays an important role on the film-surface smoothness. However, the film roughness is not significantly improved with a hydration-water concentration greater than 1.50. The SEM images show that the porosity of $CH_3NH_3PbI_3$ films tend to increase with increasing hydration-water concentration, indicating that excess hydration water may have a negative effect on the film quality.

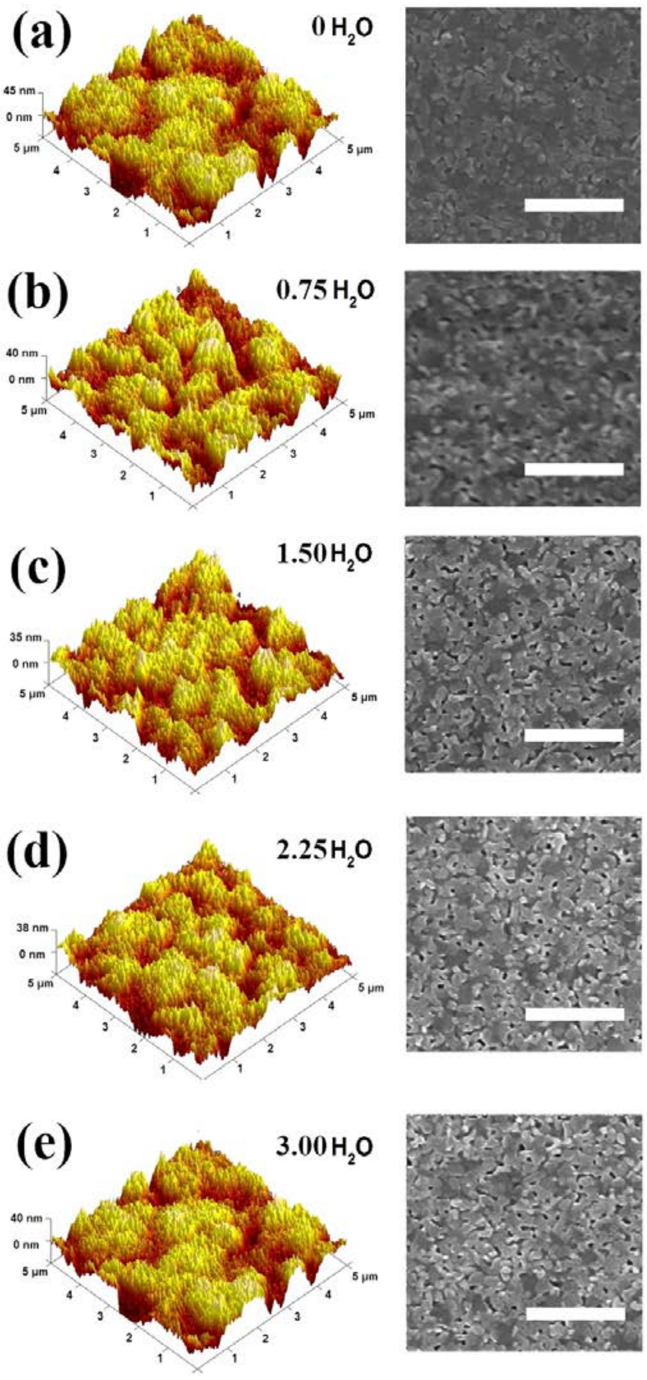

Fig. 1. Surface Morphology and RMS roughness of hydration-water-improved $CH_3NH_3PbI_3$ films measured using AFM (left) and SEM (right). The scale bar for SEM is 1 µm.

The XRD patterns of $CH_3NH_3PbI_3$ films are shown in Fig. 2. They show that all samples have a good crystalline profile. Recent reports have established that $CH_3NH_3PbI_3$ can exhibit a cubic ($Pm\tilde{3}m$) phase at high temperature and a tetragonal ($I4/mcm$) phase at room temperature [35, 36]. Our results indicate that the $CH_3NH_3PbI_3$ films prepared using $PbAc_2$ are in the tetragonal phase [37, 38]. A majority of the (110) plane and a very small portion of the (002) plane for the tetragonal phase can be observed in Fig. 2(b). The samples also contain small quantities of PbI_2 (2 orders of magnitude lower than the $CH_3NH_3PbI_3$ peak), which may originate from the annealing process or the degradation of perovskite.

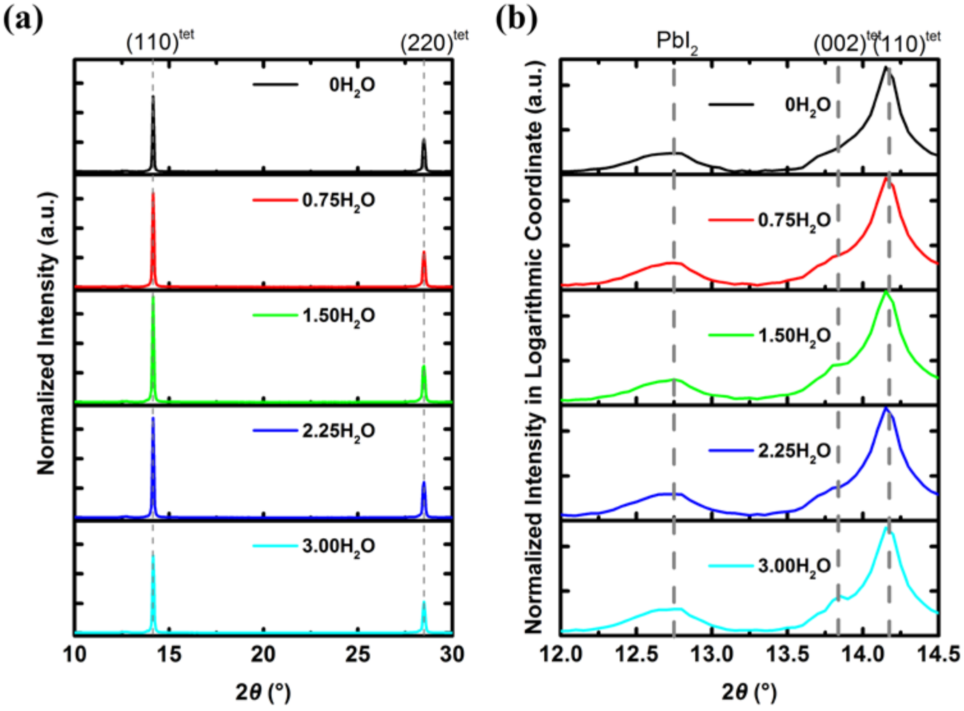

Fig. 2. XRD spectra of CH3NH3PbI3 films.

The ellipsometric spectra collected at a fixed incident angle of 65° were fitted to an optical model consisting of semi-infinite quartz substrate/ PEDOT: PSS buffer layer/ $CH_3NH_3PbI_3$ layer/ roughness layer/ ambient air based on the structure of the fabricated $CH_3NH_3PbI_3$ films. The surface-roughness layer is modeled on a Bruggeman effective medium approximation (EMA) with a mixture of 50% $CH_3NH_3PbI_3$ and 50% voids [39]. To obtain the accurate dielectric constants of each layer, the ellipsometric spectra were collected for the quartz substrate, quartz/ PEDOT: PSS, and the final $CH_3NH_3PbI_3$ films, respectively [18]. The dielectric functions of $CH_3NH_3PbI_3$ are described by the Tauc-Lorentz model [40]. The imaginary part (ε_2) is obtained from the Tauc joint density of states and the Lorentz oscillator as follows:

$$\begin{aligned}\varepsilon_{2TL}(E) &= \frac{ACE_{\mathrm{p}}(E-E_g)^2}{(E^2-E_{\mathrm{p}}^2)^2+C^2E^2}\bullet\frac{1}{E} \quad (E>E_g)\,, \\ &=0 \quad (E\le E_g)\ ,\end{aligned} \tag{4}$$

where A is the amplitude parameter, E_{p} is the peak transition energy, C is the broadening term, and E is the photon energy. The real part (ε_1) of the dielectric function can be obtained through Kramers-Kronig integration:

$$\varepsilon_1(E) = \varepsilon_\infty + \frac{2}{\pi} P \int_{E_g}^{\infty} \frac{\xi \varepsilon_2(\xi)}{\xi^2 - E^2} d\xi \,, \tag{5}$$

where P is the Cauchy principal part of the integral and ε_∞ is the constant contribution to ε_1 at high frequency. Four Tauc-Lorentz oscillators were used to construct the dielectric functions of $CH_3NH_3PbI_3$. The Tauc gap E_g was kept constant for all oscillators. The ε_∞ value of all samples is set to 1.0. The fitting of all $CH_3NH_3PbI_3$ samples displays good agreement with collected data. Figure 3 illustrates the hydration-water dependence of the complex refractive index and dielectric constants of $CH_3NH_3PbI_3$ films. The measured dielectric constants and XRD patterns indicate that the final composition of perovskite films remains constant. It can be seen from Figs. 3(a) and 3(c) that $CH_3NH_3PbI_3$ films prepared with a low-hydration precursor have higher ε_1 and n in the low-energy range. In the transparent range, where ε_2 is 0, the static dielectric constant is given by [27]

$$\varepsilon_s = 1 + \frac{\sum_i q_i l_i}{\varepsilon_0 E_f} \,, \tag{6}$$

where q_i and l_i are the electric charge of the electric dipole and distance between the charge pair in the material. ε_0 is the free-space permittivity, and E_f is the electric field. The XRD patterns in Fig. 2 indicate that the structure parameters of all samples are identical; thus, refractive-index variation induced by atomic and electric polarization can be neglected. As previously reported, $CH_3NH_3PbI_3$ is filled with different percentages of voids [20] because of the evaporation of moisture during the fabrication process of $CH_3NH_3PbI_3$ films. Therefore, a high content of hydration water will result in a $CH_3NH_3PbI_3$ sample with high porosity and low refractive index. The SEM images in Fig. 2 show a similar result.

Table 1. Dielectric Function Parameters of $CH_3NH_3PbI_3$ Films in Units of eV

		Sample				
Oscillator	**Parameter**	**$0H_2O$**	**$0.75H_2O$**	**$1.50H_2O$**	**$2.25H_2O$**	**$3.00H_2O$**
	E_g	1.592	1.595	1.598	1.581	1.590
1	E_{p1}	1.600	1.604	1.608	1.611	1.602
	C_1	0.089	0.077	0.072	0.139	0.083
	A_1	83.104	94.378	99.259	50.218	81.479
2	E_{p2}	2.564	2.547	2.538	2.539	2.526
	C_2	0.188	0.151	0.145	0.101	0.092
	A_2	1.023	0.633	0.472	0.483	0.301
3	E_{p3}	3.216	3.213	3.221	3.174	3.167
	C_3	0.676	0.416	0.377	0.580	0.394
	A_3	5.045	2.276	1.878	2.925	1.298
4	E_{p4}	4.139	4.019	4.080	4.158	4.014
	C_4	8.289	6.893	8.112	7.172	7.157
	A_4	70.386	72.142	77.099	64.405	69.910

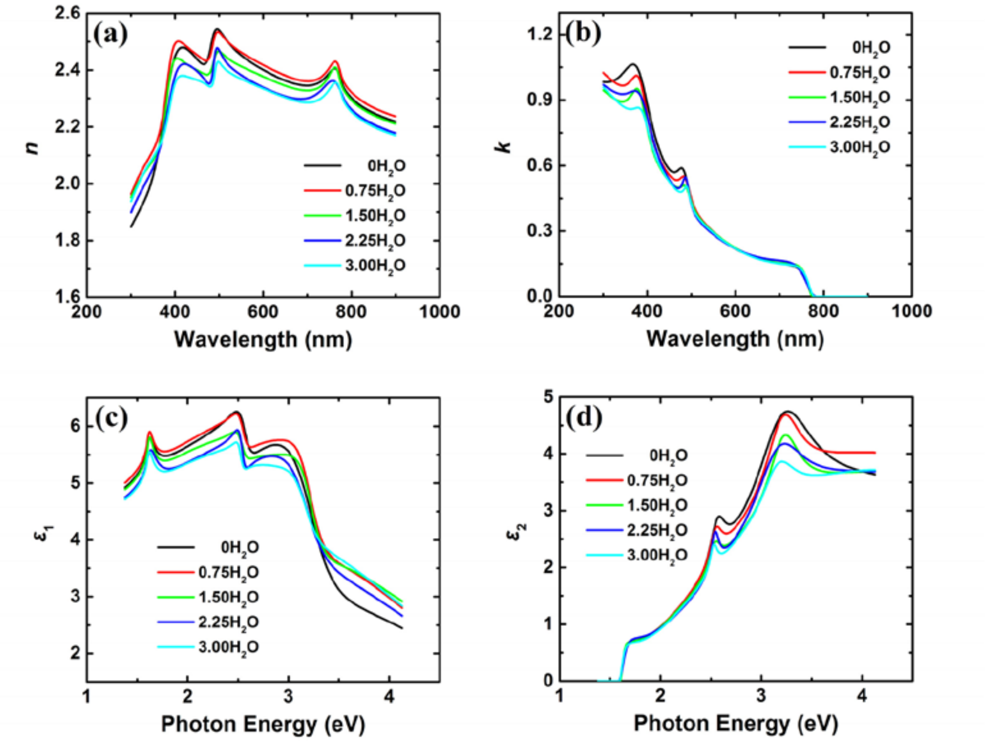

Fig. 3. Measured (a)&(b) complex refractive index and (c)&(d) dielectric constants of $CH_3NH_3PbI_3$ films.

To further understand the measured dielectric constants in Fig. 3, we list the fitted parameters of $CH_3NH_3PbI_3$ samples in Table 1. It can be seen that the band gap of $CH_3NH_3PbI_3$ films is approximately 1.6 eV, which is consistent with previous reports [18, 24]. This band gap is the difference between the valence-band maximum and conduction minimum of $CH_3NH_3PbI_3$ [24, 41]. The calculated Urbach energy of five samples are in the range of 12-14 meV, which indicates the formation of suppressed tail states in all $CH_3NH_3PbI_3$ samples. Absorption peaks at 2.5 eV are also observed in our measurement, which can be attributed to another direct transition in $CH_3NH_3PbI_3$ [18]. It has been reported that PbI_2 has a sharp transition peak at 2.5 eV, while the $CH_3NH_3PbI_3$ peak is broad [42]. The deceasing broadening term C_2 indicates that a higher level of hydration water results in a higher content of PbI_2 in perovskite films. The transition peak at approximately 3.2 eV is not as sharp as that reported by M. Shirayama et al. [18]. This is probably due to the different sample preparation method employed here; the deliberately introduced moisture reduced the ε_2 value of $CH_3NH_3PbI_3$. The last oscillator located at approximately 4 eV varies among different samples. This is due to inaccurate ellipsometric data at the short wavelength range induced by light scattering and depolarization. The measured extinction coefficient (k) decreases with the increasing content of hydration water. We attribute this phenomenon to the light scattering caused by the high surface roughness and the non-void structure formed by the fully dehydrated precursor [18]. It should be noted that, although a high roughness can benefit the absorption of the perovskite layer, it may also result in more defects to solar cells.

Based on the obtained complex refractive index, the efficiency limit of $CH_3NH_3PbI_3$ perovskite thin-film solar cells was calculated with a detailed balance model [17, 43, 44]. In the detailed balance model, the short-circuit photocurrent density J_{sc} of an illuminated solar cell is given by

$$J_{\mathrm{sc}} = q\int_0^\infty a(\lambda, L)\frac{\Gamma_{\mathrm{AM1.5G}}(\lambda)}{E(\lambda)}d\lambda \ , \tag{7}$$

where q is the elementary charge, $\Gamma_{\mathrm{AM1.5G}}$ is the AM1.5 solar flux, E is the corresponding photon energy, and $a(\lambda, L)$ is the absorptivity, which can be simulated from the film thickness L and absorption coefficient α. The dark saturation current density J_0 is formulated as

$$J_0 = q\int_0^\infty a(\lambda, L)\frac{\Gamma_0(\lambda)}{E(\lambda)}d\lambda \ , \tag{8}$$

where $\Gamma_0(\lambda)$ is the thermal emission spectrum of the absorber layer, which can be calculated from the law of black-body radiation. The open-circuit voltage V_{oc} is hence determined by

$$V_{\mathrm{oc}} = \frac{k_{\mathrm{B}}T}{q}\ln\left(\frac{J_{\mathrm{sc}}}{J_0}+1\right) \ , \tag{9}$$

where k_{B} is the Boltzmann constant and T is the working temperature of solar cells. Here, we assume $T = 300$ K and absorber thickness $L = 300$ nm.

The simulated values of J_{sc} and V_{oc} for all samples are approximately 28.5 mA/cm^2 and 1.32 V, respectively. Owing to the identical band gap and high absorption coefficient, the calculated J_{sc} and V_{oc} for different samples are essentially consistent. We also prepared several planar heterojunction solar cells to compare experimental results with the simulation results. The measured J-V curves of selected solar cells in Fig. 4(a) show that the performance of $\mathrm{CH_3NH_3PbI_3}$ solar cells strongly depend on hydration water. As illustrated in Fig. 4(b), the V_{oc} values of the prepared solar cells increase with increasing level of hydration water, and the short-circuit photocurrent density J_{sc} reaches the maximum value at $x = 1.50$. The low V_{oc} values of our solar cells can be attributed to surface defect levels and metallic contacts [45, 46], which were not considered in the simulation with the detailed balance model. The deviation among five samples indicates that the performance of perovskite solar cells is still influenced by hydration water. As all the solar cells have the same structure, the difference must originate from the perovskite films and is related to the content of hydration water in the precursor.

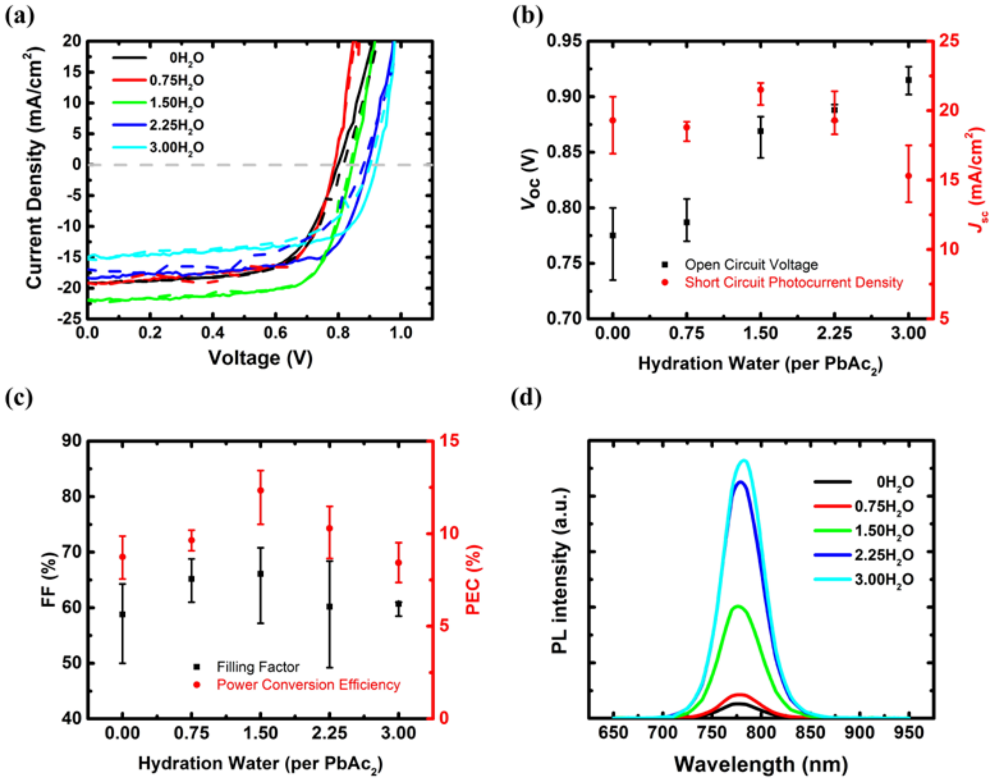

Fig. 4. (a) Measured *J-V* curves of the selected planar heterojunction configuration for $CH_3NH_3PbI_3$ solar cells. The solid and dashed lines indicate the forward and backward scanned data, respectively. (b)&(c) The performance of all fabricated solar cells. The plot indicates the average value, and the error bar indicates the upper and lower bounds of measured data. (d) Measured PL spectra of $CH_3NH_3PbI_3$ films.

To understand the difference between experiment and simulation, we further measured the PL spectra of $CH_3NH_3PbI_3$ films. As shown in Fig. 4(d), the PL emission peaks are located in the band gap of $CH_3NH_3PbI_3$ and originate from the recombination of charge carriers. The hydration water can significantly enhance the PL intensity, indicating that the introduction of hydration water can suppress the formation of non-radiative pathways in $CH_3NH_3PbI_3$ films to result in longer carrier lifetimes [26]. Considering Rau's reciprocity relation [47], the dark-current density in Eq. (8) can be rewritten as

$$J_0 = \frac{q}{\eta_{\mathrm{EL}}}\int_0^\infty a(\lambda, L)\frac{\Gamma_0(\lambda)}{E(\lambda)}d\lambda\ , \tag{10}$$

where η_{EL} is the absolute quantum efficiency of electroluminescence (EL). As previously reported, the PL emission in $CH_3NH_3PbI_3$ solar cells originates from the same type of charge pairs as in EL, and their efficiencies are approximately proportional to the PL emission [48]. If we replace η_{EL} with the PL efficiency η_{PL}, the open-circuit voltage difference ΔV_{oc} can be obtained as

$$\begin{aligned}\Delta V_{\mathrm{OC}} &= \frac{k_{\mathrm{B}}T}{q}\ln[(\frac{J_{\mathrm{SC,1}}}{J_{0,1}}+1)/(\frac{J_{\mathrm{SC,2}}}{J_{0,2}}+1)] \ , \\ &\approx \frac{k_{\mathrm{B}}T}{q}\ln(\frac{J_{0,2}}{J_{0,1}}) \approx \frac{k_{\mathrm{B}}T}{q}\ln(\frac{\eta_{\mathrm{PL,1}}}{\eta_{\mathrm{PL,2}}}) \ ,\end{aligned} \tag{11}$$

As indicated in Table 2, the calculated ΔV_{oc} between $0H_2O$ and $3.00H_2O$ $CH_3NH_3PbI_3$ solar cells is approximately 0.074 V, which is less than the value obtained in the experiment. This discrepancy probably results from the fact that the PL measurements are performed under the thin-film condition, while V_{oc} is collected for solar-cell devices. Furthermore, the different values of film-surface roughness may also affect the contact resistance.

Table 2. ΔV_{oc} of Perovskite Solar Cells with Different Hydration Water Concentration

	Sample			
ΔV_{oc} (V)	**$0.75H_2O$ $0H_2O$**	**$1.50H_2O$- $0.75H_2O$**	**$2.25H_2O$- $1.50H_2O$**	**$3.00H_2O$- $2.25H_2O$**
Calculation	0.012	0.041	0.019	0.002
Experiment	0.012	0.082	0.019	0.027

The short-circuit photocurrent density J_{sc} depends on various factors in the $CH_3NH_3PbI_3$ layer, such as roughness, non-radiative pathway, and porosity. For $0H_2O$ and $0.75H_2O$ samples, the high roughness and non-radiative pathway makes the J_{sc} values less than that for the $1.50H_2O$ sample. The $2.25H_2O$ and $3.00H_2O$ samples have higher radiative recombination efficiency, but the high porosity in the absorbing layer influenced the output current density by blocking the transport of electrons and holes. However, the $1.5H_2O$ sample has a good balance between the non-radiative pathway and porosity, and it has the highest PCE among all samples.

4. Conclusion

In summary, the optical and structure properties of hydration-water-improved $CH_3NH_3PbI_3$ perovskite films were studied using SE and PL measurements. The measured optical constants show that the band gap of the prepared $CH_3NH_3PbI_3$ films is approximately 1.6 eV, which is insensitive to the content of hydration water in the precursor, while the content of PbI_2 may increase with increasing hydration-water concentration. The SE and PL results indicate that, although hydration water can reduce the non-radiative pathway in the perovskite film, it increases porosity, which leads to a complex variation of PCE. Although the efficiency limitation can be predicted with a detailed balance model, the performance of perovskite solar cells is limited by the film quality. Solar cells based on $CH_3NH_3PbI_3$ with different hydration-water concentrations were fabricated, and their measured *J-V* curves show that hydration water in perovskite precursors favors the formation of a radiative pathway in $CH_3NH_3PbI_3$ films and leads to a higher open-circuit voltage. Simulations with the Rau's reciprocity relation also agree with the experiments. Therefore, the hydration-water concentration is confirmed to play an important role in $CH_3NH_3PbI_3$ films by influencing the surface roughness, non-radiative pathway, and film porosity. We found that the best hydration-water concentration is $x = 1.50$ for the $3CH_3NH_3I{:}1PbAc_2{\bullet}xH_2O$ precursor solution. The results reported in this work provide a guideline for further optimization of the performance of perovskite thin-film solar-cell devices by using hydration water.

Funding

National Natural Science Foundation of China (NSFC) (11174058, 61275160, 11104037, 11374055, and 61575048); No. 2 National Science and Technology Major Program of China (2011ZX02109-004); Program of China Scholarships Council (201606100168).